Journal Pre-proof

Enabling the ability of Li storage at high rate as anodes by utilizing natural rice husks-based hierarchically porous SiO_2/N-doped carbon composites

Yi Feng , Li Liu , Xiaoyang Liu , Yifei Teng , Yixin Li , Yutong Guo , Yanchao Zhu , Xiaofeng Wang , Yimin Chao

PII: S0013-4686(20)31326-8
DOI: https://doi.org/10.1016/j.electacta.2020.136933
Reference: EA 136933

To appear in: *Electrochimica Acta*

Received date: 21 June 2020
Revised date: 10 August 2020
Accepted date: 10 August 2020

Please cite this article as: Yi Feng , Li Liu , Xiaoyang Liu , Yifei Teng , Yixin Li , Yutong Guo , Yanchao Zhu , Xiaofeng Wang , Yimin Chao , Enabling the ability of Li storage at high rate as anodes by utilizing natural rice husks-based hierarchically porous SiO_2/N-doped carbon composites, *Electrochimica Acta* (2020), doi: https://doi.org/10.1016/j.electacta.2020.136933

Enabling the ability of Li storage at high rate as anodes by utilizing natural rice husks-based hierarchically porous SiO_2/N-doped carbon composites

Yi Feng[a], Li Liu[b,c], Xiaoyang Liu[a], Yifei Teng[a], Yixin Li[a], Yutong Guo[a], Yanchao Zhu[a], Xiaofeng Wang[a,b,*] & Yimin Chao[b,*]

[a]*State Key Laboratory of Inorganic Synthesis and Preparative Chemistry, College of Chemistry, Jilin University, Changchun, China*

[b]*School of Chemistry, University of East Anglia, Norwich Research Park, Norwich NR4 7TJ, UK*.

[c]*Department of Chemistry, Northeast Normal University, Changchun 130024, China*

**Email: wangxf103@jlu.edu.cn; Y.Chao@uea.ac.uk*

Yi Feng: Data Curation, Methodology, Writing - Original Draft.

Li Liu: Formal analysis.

Xiaoyang Liu: Validation.

Yifei Teng: Software.

Yixin Li: Investigation.

Yutong Guo: Visualization.

Yanchao Zhu: Resources.

Xiaofeng Wang: Supervision, Project administration, Writing - Review & Editing.

Yimin Chao: Conceptualization.

Abstract

One of the greatest challenges in developing SiO_2/C composites as anode materials in lithium ion batteries (LIBs) is to improve the ability of Li storage at high rate over long-term cycles. Herein, biomass rice husks-based hierarchically porous SiO_2/N-doped carbon composites (BM-RH-SiO_2/NC) were prepared by ball mill and thermal treatment. BM-RH-SiO_2/NC can still retain a reversible capacity of 556 mAh g^{-1} over 1000 cycles at a high current of 1.0 A g^{-1}. At 5.0 A g^{-1} the capacity is kept as high as 402 mAh g^{-1}. This impressively long-term cyclic performance and high-rate capability of BM-RH-SiO_2/NC can be ascribed to the synergetic effect between the natural SiO_2 nanoparticles (< 50 nm) and the NC layer. The coating NC layer can not only effectively mitigate the volume strain during charge-discharge process to offer stably cyclic performance but also improve the electrical conductivity. Furthermore, the hierarchical porosity and better electrolyte wettability offer the rapid Li^+ diffusion and electron transfer, which enhance the pseudocapacitive behavior of whole electrode material and then guarantee fast electrochemical kinetics. Importantly, the unique Li-storage mechanism of active SiO_2 in BM-RH-SiO_2/NC composite was formed and found, which further validates the improved electrochemical capability.

Keywords: Rice husks; SiO_2/N-doped carbon; Hierarchical porosity; Li-storage mechanism; Electrochemical performance

1. Introduction

Over the past decades, owing to the high energy density and long lifespan [1-3], the rechargeable lithium-ion batteries (LIBs) have obtained overwhelming commercial applications ranging from portable electronics to hybrid vehicles [4, 5]. As the increasing demand for quick charge-discharge of LIBs, the high-power density is extremely desirable, meaning the excellent rate performance in the design of electrode materials for the LIBs.

Among the diverse candidates of the anode materials for LIBs, silica is considered as a promising anode material in terms of its relatively high theoretical capacity (up to 1965 mAh g^{-1}) and low discharge potential (below 0.7 V) [6, 7]. The Al doped porous C/SiO_2 composites via a high-temperature solid-state method by Cui et al.[8] can still receive a capacity of 1085.1 and 671.3 mAh g^{-1} at the current densities of 0.2 and 1.0 A g^{-1}, respectively, which is higher than that of P-based anode material (908.1 and 556.6 mAh g^{-1}) [9]. Liu et al. [10] reported that SiO_2/Ni hierarchical hollow spheres displayed excellent rate performance, especially the high specific capacity of 337 mAh g^{-1} after 1000 cycles at 10 A g^{-1}, which is much higher than that of SnO_x-based material counterpart [11]. These results demonstrate that silica-based materials with high Li-storage at high rate can serve as the promising electrode materials for high-power density LIBs compared with the other prevailing anode material. Meanwhile, several intrinsic drawbacks still need to be overcame, such as poor electrical conductivity, large volume change during charge-discharge process and the sluggish electrochemical kinetics

[12-14]. The common approach is to combine the carbonaceous materials with silica in order to improve the electrical conductivity and to alleviate the volume change. Li et al. reported the nanosilica/carbon spheres via in-situ copolymerization [15], exhibiting a capacity of 620 mAh g^{-1} after 100 cycles at 0.1 mA g^{-1} and a capacity of 350 mAh g^{-1} after 10 cycles at a larger current of 0.6 mA g^{-1}. Wang et al. prepared the SiO_2/C/CNTs composites through an in-situ chemical vapor deposition (CVD) strategy. With the current densities at 0.05 A g^{-1} and 1.0 A g^{-1} the corresponding unstable capacity is 500 mAh g^{-1} over 100 cycles and 315 mAh g^{-1} after 1000 cycles [16]. Nita et al. prepared the carbon/SiO_2 hybrid materials with interpenetrating network, in which tetraethyl orthosilicate (TEOS) was chosen as the precursor and the size of the synthesized SiO_2 particles is 2-5 nm. The capacity of as-obtained carbon/SiO_2 is 535 mAh g^{-1} at the rate of 0.2 C (ca. 0.7 A g^{-1}) [17]. The decent cyclic behaviors of SiO_2/C composites mentioned above have been achieved at low current density with limited cyclic numbers, but the cyclic property at large current is still not good enough. Liang et al. reported the SiO_2/C composites with submicron SiO_2 particles embedded in porous carbon. With a carbon content of 14 wt%, the SiO_2/C composite showed the optimal electrochemical behavior. The capacities are 620 mAh g^{-1} at 0.1 A g^{-1} and 534 mAh g^{-1} at 1.0 A g^{-1} over 1000 cycles [18]. The improvement in stability is aided by carbon coating, but the mechanism and electrochemical kinetics of Li-storage are remained unclear.

The carbon matrix in silica/carbon composites could be further modified by the heteroatom nitrogen. The high electronegativity of nitrogen can enable a strong interaction between the N-doped carbon (NC) and Li ions [19]; Meanwhile, there are more defects generated by replacing carbon atoms with nitrogen atoms, providing more reaction sites with lithium ions. The Li-storage capacity should be enhanced by these additional reactions. Additionally, the presence of N heteroatom is able to improve the electrical conductivity and electrolyte wettability of electrode material [20]. Liang et al. synthesized the N-doped mesoporous C/SiO_2 composites (N-C/SiO_2) via a multi-constituent co-assembly method , and demonstrated a higher specific capacity than the sample without N-doping [21].

Generally, the TEOS, silicate and commercial SiO_2 are served as silica source during the preparation of SiO_2/C composites. Recently, lots of experiments employed biomass as the silica source due to environmental considerations. Among the various biomass materials, rice husks (RHs) have been widely applied in the LIBs [22-28]. The SiO_2 exists in RHs (RH-SiO_2) in the form of uniform nanoscale structure and coated by organic carbon component. The porous structures of RH-SiO_2 are formed during the natural growth process of rice [29], that allows RHs to be processed into a promising SiO_2-based anode material. However, reported results on the RHs-based composites are still short of excellent cyclic performance at the high rate.

In this work, the simple nitrogen doping, toward rice husk derived SiO_2/C, facilitates the fast electrochemical kinetics, leading to the impressive capability of Li-storage at the high rate over long-term cycles, Moreover, the unique Li-storage mechanism, that the routines of reversible capacity contribution of active SiO_2 in composite are different, was firstly proposed and discussed in detail.

2. Experimental Section

2.1 Materials Fabrication

After grinding and washing with water, the RHs (obtained locally in Changchun, Jilin, China) were immersed in 1M HCl at 100 ℃ for two hours to eliminate the metal impurities, and then were collected by filtration and washing with deionized water, drying at a temperature of 120 °C overnight. Subsequently, RHs were calcined in Ar gas at 650 ℃ for 2 h with a heating rate of 5 ℃ min^{-1}. Naturally cooled to room temperature, the powder (RH-SiO_2/C) and silicon nitride balls (10 mm) were transferred to the silicon nitride vial to perform the mechanical milling for 6 h at a rotating speed of 800 rpm. For the N-doping process, 0.4 g as-obtained composites (BM-RH-SiO_2/C) and 0.5 g urea were fully mixed and ground in a mortar for 30 min. Afterwards, the mixture was placed in a quartz crucible and heated in a tube furnace under Ar gas flow at 650 °C for 1 h with the ramp rate of 3 ℃ min^{-1}. After cooling down to room temperature, the N-doped composites (BM-RH-SiO_2/NC) were obtained. For comparison, the original RH-SiO_2/C was also doped with nitrogen via the same method (named as RH-SiO_2/NC). And the BM-RH-SiO_2/C was applied as another control sample without any N-doping treatment.

Additionally, the experimental parameters of N-doping including the urea usage and thermal temperature, were investigated systematically in which the details are listed in Table S1.

2.2 Materials Characterization

The phase structure of the materials was investigated by X-ray diffraction (XRD) on a D/MAX2550 diffractometer with Cu Kα radiation and Raman spectroscopy (INVIA, England). Scanning electron microscope (SEM, JSM-6700F) and transmission electron microscope (TEM, Tecnai G2 S-Twin F20) with element mapping images were used to examine the morphological structures of the products. X-ray photoelectron spectroscopy (XPS, ESCALAB250) was employed to study the compositions as well as the chemical states of the products. The FTIR spectra of the samples were recorded at room temperature using an IFS-66V/S with the KBr disk method. Nitrogen adsorption and desorption isotherms were investigated at 77 K using an ASAP 2420 surface area analyzer in order to obtain the specific surface area basing on the BET model and the pore size distribution (PSD) by applying the Density Functional Theory (DFT) method. The contact angle of electrode was measured on Kruss DSA30 contact angle system at room temperature.

2.3 Electrochemical Measurements

The working electrodes were fabricated by casting slurry containing active material, conductive additive (acetylene black) and binder (polyvinylidene fluoride) with a weight

ratio of 8:1:1 on copper-foil current collector, followed by drying in a vacuum oven at 80 ºC for 12 h. The electrochemical properties of the as-prepared samples were carried out using 2025 coin-type cells assembled in an argon-filled glovebox (<0.2 ppm of oxygen and water). Lithium metal was applied as the counter electrode, the microporous membrane (Celgard 2500) as separator and 1 M $LiPF_6$ in the dimethyl carbonate/ethylene carbonate (1:1 v/v) as the electrolyte. Galvanostatic charge-discharge profiles, the cycle life and rate capability tests were performed using a Neware battery test system within the voltage range of 0.01-3.0 V (vs. Li^+/Li). Cyclic voltammetry (CV) at various sweep rates of 0.1-1.5 mV s^{-1} and electrochemical impedance spectroscopy (EIS) analysis with a voltage amplitude of 5 mV in the frequency range from 100 kHz to 0.01 Hz were both conducted on CHI 760D electrochemical workstation. After charge-discharge process, the electrodes were soaked in dimethyl carbonate for two days and subsequently dried in a vacuum chamber for 12 h prior to the SEM, XPS and TEM measurements.

3. Results and discussion

As shown in the Scheme 1, the RHs were processed by water-washing and acid-leaching to remove the dust and metal oxides before further synthesis procedure. After the carbonization under inert gas atmosphere, the original RH-SiO_2/C was obtained. As shown in the SEM images of Fig. S1a and S1b, there is a distinctly nonuniform

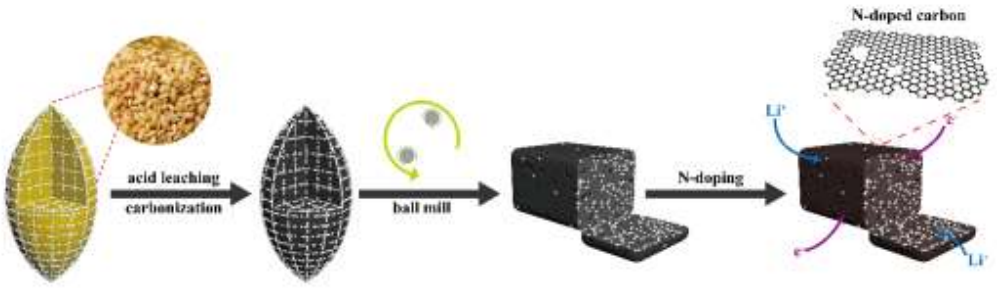

Scheme 1. Synthesis procedure of hierarchically porous SiO_2/N-doped carbon composites.

between the smooth carbon blocks deriving from organic components and aggregated silica nanoparticles, which inherit from the original texture of RHs. In fact, the diameter of monodispersed SiO_2 spherical particle is measured as 20-50 nm (Fig. S1b), which is believed to be favor of electrochemical performance. But the particles agglomeration and uneven dispersion issues between silica and carbon should be solved. The differences in hardness and interface energy between carbon and silica can offer a reasonable strategy to process the composite via ball mill [3]. During the mechanical ball milling process, the powder particles are repeatedly collided, mixed, fractured and rewelded by milling balls and milling jar, which can decrease the grain sizes of aggregated silica and carbon block, and fabricate the embedded architecture of neighboring SiO_2 and C. As displayed in Fig. 1a and 1d, after ball mill the BM-RH-SiO_2/C exhibits a completely different morphology. The carbon blocks are broken into micro-sized feature with rough and compact surface and nanosized silica

particles have been covered in the carbon matrix. The EDS mappings of Si, O and C in large region for Figure 1a-1c are displayed in Fig. S2. The RH-SiO_2/NC without ball mill is different from the BM-RH-SiO_2/C and BM-RH-SiO_2/NC via recognizing the signals of between C and Si or O elements, in which there is the distinguishably uneven distribution between silica and carbon. The mechanism and significance of ball mill have been given and analyzed in detail in our previous work [3]. More importantly, the shear force generated from ball mill encourages the formation of more active carbon radicals that can react with the air in the ball milling jar and then introduce the more oxygen functional groups on the surface of carbon [30, 31], which is favor of the nitrogen atoms introduction. After N-doping treatment, the as-obtained BM-RH-SiO_2/NC composites (Fig. 1c and 1f) show no obviously morphological distinction compared with BM-RH-SiO_2/C, except for the looser contact among the particles.

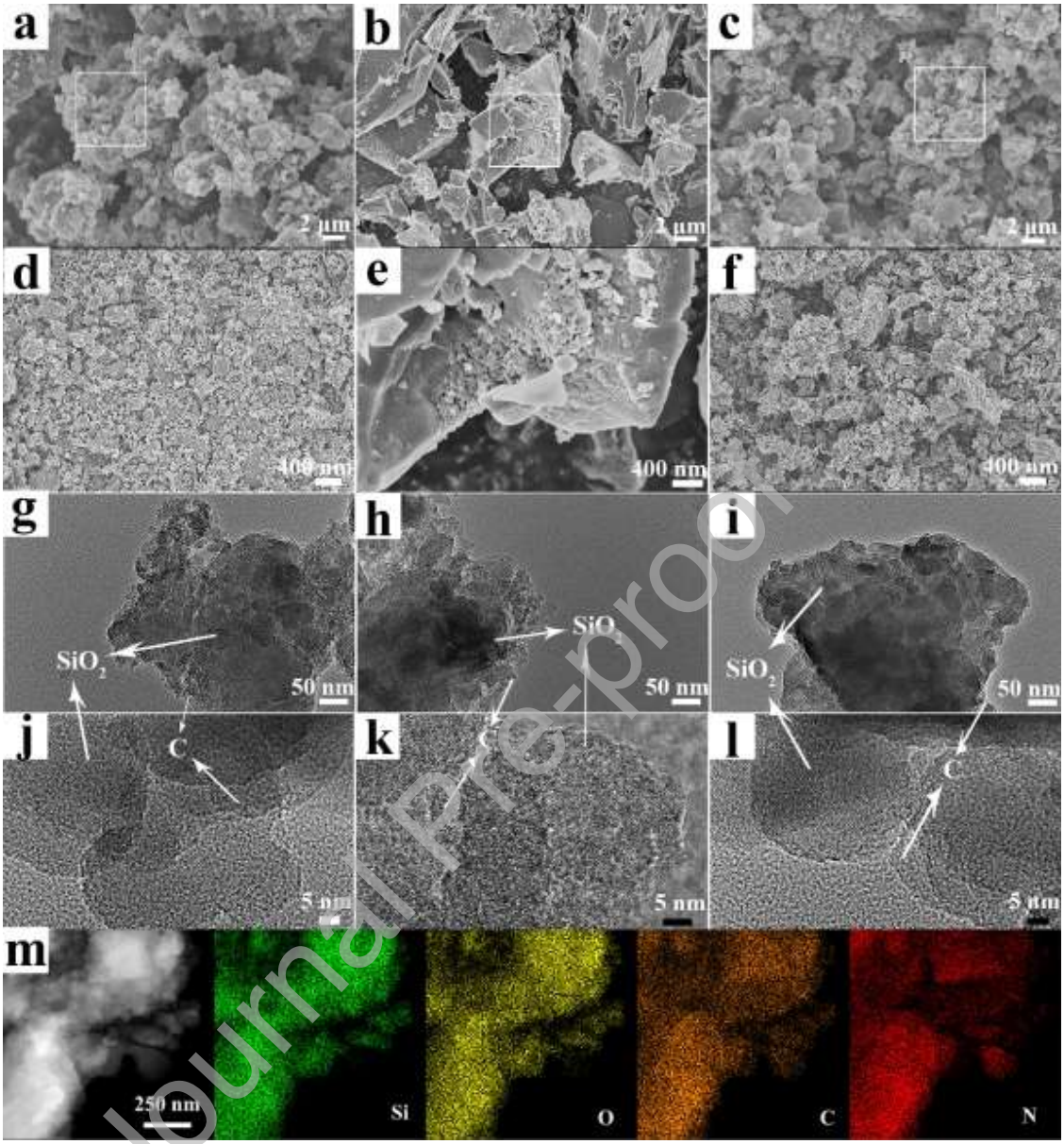

Fig. 1. SEM images of (a, d) BM-RH-SiO_2/C, (b, e) RH-SiO_2/NC and (c, f) BM-RH-SiO_2/NC; TEM images of (g, j) BM-RH-SiO_2/C, (h, k) RH-SiO_2/NC and (i, l) BM-RH-SiO_2/NC; (m) EDS mapping of BM-RH-SiO_2/NC.

However, in the case of RH-SiO_2/NC without ball mill (Fig. 1b and 1e), the surface of carbon blocks become rougher and the aggregated silica particles are exfoliated from

carbon matrix, but which remains the inhomogeneous dispersion of silica particles in carbon component. Moreover, the new detectable nanopores are generated during the N-doping treatment. These changes are also observed in TEM images and further confirmed by the EDS mapping. The elements of Si, O, C and N present the homogeneous distribution and also state the high-content introduction of N atom in BM-RH-SiO_2/NC composite (Fig. 1m), while the signals of corresponding elements in RH-SiO_2/NC sample without ball mill are indictive of the slightly uneven dispersion between silica and carbon and the smaller N-doping level (Fig. S1c). Therefore, the ball mill prior to N-doping process is indispensable for the fine distribution of SiO_2 in carbon matrix and the nitrogen doping.

As shown in Fig. S3, the XRD patterns of as -obtained samples were performed to analyze the crystal phase. Similar diffraction features are observed from all samples. The two broad diffraction peaks located in 23° and 43° of the 2θ range are indicative of the amorphous SiO_2 and carbon in all samples [32]. The peak at 43° from BM-RH-SiO_2/NC is the weakest, confirming the most defect-rich feature of the carbon component [33]. In the Raman spectra (Fig. S4) of the corresponding products, the peak located around 1350 cm^{-1} refers to D-band of carbon and the peak at 1590 cm^{-1} is G-band, which stand for the defect

of carbon and sp^2-carbon domains, respectively. The value of I_D/I_G ratio can be used to evaluate the degree of the disorder of carbon [34-38]. The I_D/I_G ratio of BM-RH-SiO_2/NC

(0.97) is higher than that of BM-RH-SiO_2/C (0.86), manifesting the more defects in the carbon matrix of BM-RH-SiO_2/NC and the nitrogen heteroatoms have been successfully introduced into BM-RH-SiO_2/NC [39, 40]. In addition, the difference of I_D/I_G ratio between RH-SiO_2/NC (0.77) and BM-RH-SiO_2/NC (0.97) illustrates that ball mill improves the disorder degree of carbon.

X-ray photoelectron spectroscopy (XPS) has been used to obtain the surface electronic state and chemical configuration. Judging from the characteristic peaks of the survey spectrum in Fig. 2a, BM-RH-SiO_2/NC is composed of O, N, C, and Si elements. As shown in Fig. 2b and 2c, high resolution XPS spectra of Si 2p at 103.8 eV and O 1s at 532.8 eV are specific for the existence of SiO_2 [41]. The C1s spectrum is divided into three characteristic peaks, where the main peak at 284.6 eV refers to the sp^2 of C=C bond and

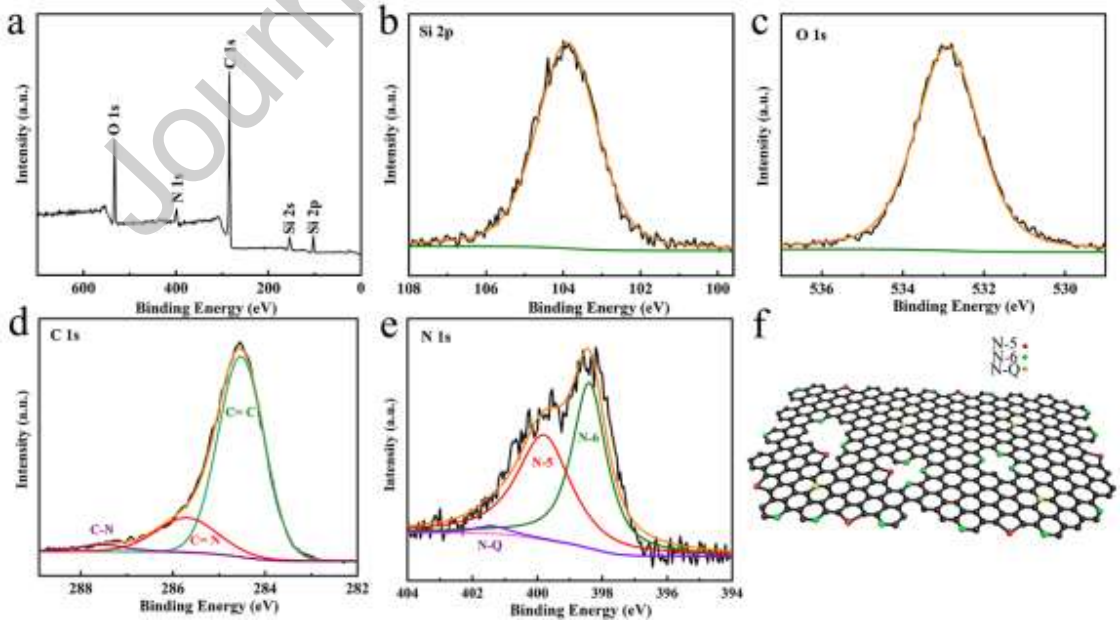

Fig. 2. XPS spectra of BM-RH-SiO_2/NC: (a) the survey spectrum, high-resolution spectra of (b) Si 2p, (c) O 1s, (d) C 1s, and (e) N 1s; (f) the schematic illustration of three nitrogen species in NC.

other two peaks around 285.8 eV and 287.5 eV are associated with C=N (sp^2) and C-N (sp^3) bonds, respectively [11, 42]. Furthermore, the N1s spectrum (Fig. 2e) is deconvoluted into three peaks [34]: pyridinic N (N-6) at 398.4 eV, pyrrolic N (N-5) at 399.8 eV and quaternary N or graphitic N (N-Q) at 400.9 eV, where the N-6 and N-5 species are predominated in N-containing functional groups. As shown in the schematic illustration (Fig. 2f), the two types of nitrogen, N-5 and N-6, are located at the edge or defect sites of carbon layer. N-6 atoms can donate one pair of lone electrons, and N-5 atoms contribute two electrons to the π system, both of which enable to endow the electron-rich state of N-doping carbon and increase the Li-storage active sites [43, 44]. The N-Q atoms are doped into the graphitic carbon plane bonds and are served as the electron carriers and donors, which improve the electronic conductivity of the integrate composite[45]. According to the results of XPS shown in Table S2, the nitrogen level of BM-RH-SiO_2/NC composite (5.12%) is higher than that of RH-SiO_2/NC (3.31%). The reason can be explained as the following two aspects: for the one thing, during the ball milling process the carbon blocks were scattered and simultaneously more carbon active sites could be exposed. For another thing, BM-RH-SiO_2/C composite (15.53%) contains more oxygen groups than that of RH-SiO_2/C (15.10%), which can be combined with the

N-precursor to introduce the nitrogen atoms. After N-doping the BM-RH-SiO_2/NC composite, with the least oxygen content, tends to relieve the decomposition of electrolyte and the surface side reactions between electrolyte and electrode [46]. Additionally, the composites under varying conditions of N-doping were also prepared and explored. As shown in Table S3, it is found that the level of N-doping increases and then tends to stabilize with the increase of urea usage. While N-amount is continuous declination when the thermal temperature increments since the elevated temperature induces removing the nitrogen doped to some extent.

In order to further gain insight into the chemical bond, the FTIR spectra of materials were produced in Fig. S5. There are similarly broad absorption bands located at 470 cm^{-1}, 800 cm^{-1} and 1104 cm^{-1} referring to the Si-O rocking vibration, Si-O bending vibration and asymmetry Si-O-Si stretching vibration, respectively, which declare the presence of SiO_2 in all samples [47]. The shoulder peak at 1200 cm^{-1} in all samples is ascribed to the Si-O-C involving the SiO_2 and C components, which indicates that silica and carbon are bonded via the covalent bond inherited from the natural interaction force between silica and lignin of RHs rather than simply physical blend, and ball milling process can' t destroy this stable chemical bond. As can be seen in Fig. S5, the BM-RH-SiO_2/C behaves relatively complicated characteristic peaks, in which the peaks at 1387 cm^{-1} and 2930 cm^{-1} correspond to C-H bond, and the peaks around 1685 cm^{-1} and 3427 cm^{-1} are assigned to the C=O and O-H stretching vibration, respectively. After N-doping in the

case of BM-RH-SiO_2/NC, the above-mentioned O-species peaks have vanished whereas the peak at 1575 cm^{-1} related with C-N bond has appeared [48-50]. These results again validate the fact that the N heteroatom has been doped into the carbon matrix of BM-RH-SiO_2/NC.

It is generally believed that the N-doping may influence the wettability of electrode material towards organic electrolyte, which is significantly crucial for electrochemical performance. As shown in Fig. 3, the contact angle was obtained by dropping water droplet

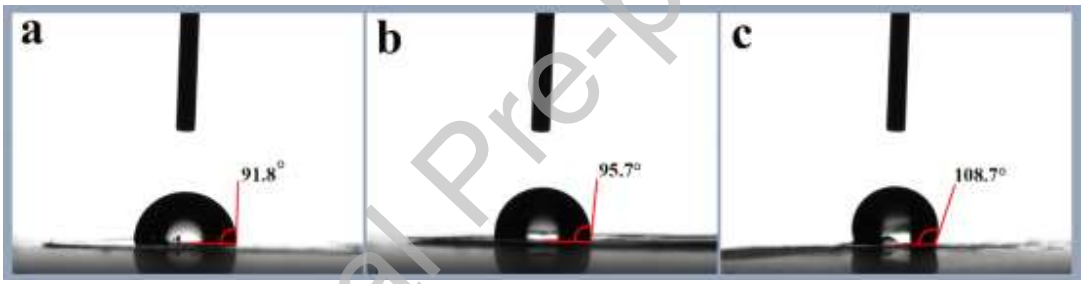

Fig. 3. The contact angles of water distributed on the surface of the electrodes of (a) BM-RH-SiO_2/C, (b) RH-SiO_2/NC and (c) BM-RH-SiO_2/NC.

into as-prepared electrode films. The contact angle of BM-RH-SiO_2/NC (108.7 °) is larger than those of RH-SiO_2/NC (95.7 °) and BM-RH-SiO_2/C (91.8 °), meaning that BM-RH-SiO_2/NC has the strongest hydrophobicity among the three electrode materials. Videlicet, the BM-RH-SiO_2/NC features the most desirable wettability toward the organic electrolyte resulting from the decrease of the oxygen-containing group functionality. The enhanced electrolyte wettability enables Li ions to easily diffuse into

the interface of electrode and electrolyte and then into the bulk electrode material [50], consequently enhancing the electrochemical property, especially the rate performance.

As seen in Fig. 4, the N_2 adsorption-desorption test was performed to evaluate the porous structure of samples. The similar curves of three samples can be classified as the type-IV isotherm with an H3 hysteresis (Fig. 4a). The relative pressure (P/P_0) has a sharp rise below 0.01 and a hysteresis loop ranging from 0.4 to 1.0, indicating the coexistence of micropores and mesopores. The capillary-condensation, the characteristic of macropores, is observed after the high relative pressure (P/P_0 = 0.9). Furthermore, the pore size distributions (PSD) of samples are given in Fig. 4b, where all the samples exhibit the distinguishing characteristic. The BM-RH-SiO_2/C possesses the microporous structure at 1.18 nm which is similar to RH-SiO_2/C (Fig. S6). As for BM-RH-SiO_2/NC, in addition to the micropore at 1.24 nm, the new micropore centered at 0.80 nm, the widening mesopore range of 27.27-46.67 nm and the visible macropore have also been observed (inset of Fig. 4b), revealing the presence of hierarchically porous structure. While the RH-SiO_2/NC, with porous structure at 1.18 nm, only has the new micropore of 0.46 nm. Therefore, the ball mill prior to N-doping treatment is critical step for sample to engineer the hierarchical porosity, and N-doping can generate the new porous structure. According to the N-doping mechanism, the gases were released, such as NH_3 and H_2O, when the as-obtained samples reacted with urea, which brings about the new microporous structure. As the amount of gas accumulating, the larger pores involving mesopore and

macropore are probably formed, meaning that the porosity of composite may be bound up the content of N-doping. This viewpoint is further verified by the texture of composites at different thermal temperatures and amounts of urea. As shown in Table S3, Table S4, Fig. S7 and Fig. S8, H-BM-RH-SiO_2/NC with the higher N-atom of 5.20% features the obvious micro- and mesoporous structure whereas the other composites containing the smaller amount of nitrogen just display the micropore. The structure of BM-RH-SiO_2/NC is rich in micro-, meso- and macropores, playing a synergistically promoting role in the Li-ion battery [20, 51, 52]: the micropore is available for the active sites of Li storage; mesopore can serve as a channel of the transfer electrolyte; and macropore is regarded as a "reservoir" of large amount of electrolyte to shorten the transport distance of Li ions. This hierarchical porosity facilitates

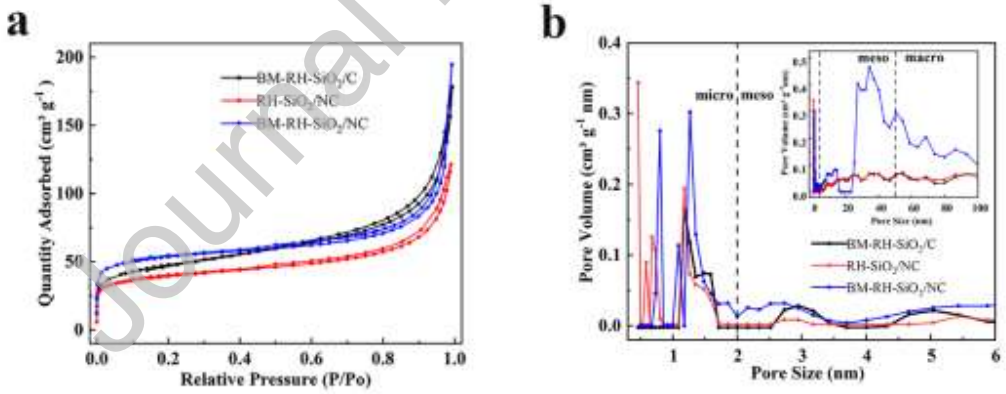

Fig. 4. (a) Nitrogen adsorption/desorption isotherm and (b) pore size distribution of samples.

Table 1. The specific surface area and pore structure of samples.

Sample	S_{BET} ($m^2 g^{-1}$)	S_{micro} ($m^2 g^{-1}$)	V_{total} ($cm^3 g^{-1}$)	V_{micro} ($cm^3 g^{-1}$)	Main pore type
BM-RH-SiO_2/C	164.44	51.06	0.28	0.02	meso-
RH-SiO_2/NC	128.00	72.74	0.20	0.03	micro-
BM-RH-SiO_2/NC	183.22	109.29	0.30	0.05	micro-, meso-

the improvement of the electrochemical properties, especially the rate capability [53].

The detailed parameters of specific surface area (SSA) and pore structure of samples have been summarized in Table 1. The SSA and pore volume of BM-RH-SiO_2/NC are both the highest among three samples. It is not hard to see the ball mill can make the SSA higher and the N-doping facilitates to create rich-micropore.

After assembled as the anode for LIBs, the charge-discharge profiles at the first cycle and the CV performances of as-prepared samples were investigated to explore the Li-storage mechanism over the circuit voltage of 0.01-3 V. There are three detectable plateaus around1.40 V, 1.15 V and 0.75 V at the initial discharge curve in all samples (Fig. 5a), which are also embodied in the first cathodic sweeps of CV plots (Fig. 5b, 5c and 5d). the prominent cathodic peak around 0.7 V can be attributed to the formation of the solid electrolyte interface (SEI) layer and the peaks about 1.1 V and 1.4 V are associated with side reactions between the electrolyte and electrode material, but these

peaks disappear in the subsequent cycles. The overlapped anodic peak about 1.2 V in the charging branches of all samples is probably related to the partial reversibility between the SiO_2 and the generating Si, as described in Eq. (1) [54]. Unlike the RH-SiO_2/NC, however, new peaks were formed for RH-SiO_2/NC at the 100^{th} cycle and BM-RH-SiO_2/NC at the 10^{th} and 100^{th} cycle, where the reduction peak at 0.14 V and the oxidation peak at 0.51 V successively correspond to Si-alloying and Li_xSi-dealloying processes [55, 56] as depicted in Eq. (2). These redox peaks are also observed in the CV curve of BM-RH-SiO_2/NC at the scan rate of 0.2 mV s^{-1} (see Fig. S9). Therefore, a novel conclusion can be drawn that after the activation process of initial several cycles the reversible capacity contribution of N-doping composites is dominated by the reaction of generating Si in Eq. (2) and BM-RH-SiO_2/NC experiences the shorter activation time than that of RH-SiO_2/NC, while the reaction of Eq. (1) plays a vital role in the reversible capacity of BM-RH-SiO_2/C. In short, the Li-storage mechanism of N-doping composites, especially for the BM-RH-SiO_2/NC, distinguishes from that of BM-RH-SiO_2/C and it is the facile N-introduction that can improve the primary Li-storage mechanism of active SiO_2 in composites. The enhanced electrical conductivity and hierarchical porosity of BM-RH-SiO_2/NC are able to realize the fast electrochemical dynamics including charge diffusion and rapid electron transfer, which renders the preferable Li-storage mechanism and the better electrochemical behavior.

$$5SiO_2 + 4Li^+ + 4e^- \leftrightharpoons 2Li_2Si_2O_5 + Si \quad (1)$$

$$Si + xLi^+ + xe^- \leftrightharpoons Li_xSi \quad (2)$$

$$SiO_2 + 4Li^+ + 4e^- \rightarrow 2Li_2O + Si \quad (3a)$$

$$2SiO_2 + 4Li^+ + 4e^- \rightarrow Li_4SiO_4 + Si \quad (3b)$$

The XPS analysis of BM-RH-SiO_2/NC electrode at the diverse charge-discharge statuses was adopted to further find out the Li-storage mechanism. As presented in Fig. S10a, the spectrum of Si 2p of the free original electrode is centered at 103.8 eV, which broadens and shifts toward 101.5 eV and 103.1 eV after discharged to 0.01V and charged to 3.0 V, respectively. It can be deduced the complicated coexistence of Li-Si alloy and silicate lithium. Moreover, the O1s peak shifts from original 532.8 eV to 531.6 eV when the electrode is discharged to 0.01 V, and it returns to 532.2 eV after charged to 3.0 V (Fig. S10b), which proves the presence of reversible $Li_2Si_2O_5$ and irreversible Li_2O or Li_4SiO_4. Therefore, the reversible reaction of BM-RH-SiO_2/NC primarily comes from the Eq. (2), accompanied by the minor Eq. (1). Simultaneously, the Eq. (3a) or Eq. (3b) leads to the irreversible capacity. HRTEM images of the worked BM-RH-SiO_2/NC electrode were applied to further determine the electrochemical reaction. As shown in Fig. S11, when the BM-RH-SiO_2/NC electrode is discharged to 0.01 V, there are Li_4SiO_4, $Li_2Si_2O_5$ and $Li_{13}Si_4$ phases. After charged to 3.0 V, the Li_4SiO_4 still exists, but not the $Li_2Si_2O_5$ phase, in the BM-RH-SiO_2/NC. Besides, the Si crystallite can be also detected. So, there are two pairs reversible reactions related to $Li_2Si_2O_5$ and $Li_{13}Si_4$ and the irreversible reaction involving Li_4SiO_4 during the Li-storage process of BM-RH-SiO_2/NC electrode.

The cycling performances of three samples at the current density of 0.1 A g^{-1} over 100 cycles were shown in Fig. 5e. The BM-RH-SiO_2/NC delivers a discharge capacity of 1373 mAh g^{-1} with the Coulombic efficiency of 63% in the first cycle, which is higher than those of the BM-RH-SiO_2/C (1026 mAh g^{-1} and 52%) and RH-SiO_2/NC (1115 mAh g^{-1} and 61%) (see Table S5). Herein, the improved discharge capacity of BM-RH-SiO_2/NC benefits from more active sites including N-6 and N-5 species and the micropores of the hierarchical porosity. The reason why the ICE can be significantly increased up to 10% is that the reduced oxygen functional group on the surface of NC can lessen the decomposition of electrolyte and side reaction between electrolyte and electrode. Undeniably, the relatively low ICE is still the major problem of the SiO_2 anode material in the full-cell application, however, the ICE of BM-RH-SiO_2/NC has already improved to be the higher level among similar products. After 100 cycles BM-RH-SiO_2/NC remains the reversible capacity of 780 mAh g^{-1} and the corresponding capacity retention is as high as 98.6% on the basis of the 5^{th}-cycle capacity (791 mAh g^{-1}). This cyclic stability is further embodied by the overlapping charge-discharge curves in the Fig. 5f. As displayed in Fig. 5g, the rate behaviors of three samples were examined for 10 cycles at each current density: 0.1, 0.2, 0.5, 1.0, 2.0 and 5.0 A g^{-1}. Compared with BM-RH-SiO_2/C, it is obvious that the N-doping process has achieved the better rate properties at each rate current. The reversible capacities of BM-RH-SiO_2/NC can reach 758, 685, 563 and 487 mAh g^{-1} at the corresponding current densities of 0.2, 0.5, 1.0 and 2.0 A g^{-1}. When the high rate increases to 5.0 A g^{-1}, meaning just five-minute discharging

time, the discharge capacity is as high as 402 mAh g^{-1}. After the current density returns to the original 0.1 A g^{-1}, the reversible capacity maintains the value of 795 mAh g^{-1}, which is indicative of the remarkable rate capability in contrast with BM-RH-SiO_2/C and the other SiO_2/C materials reported in the previous literatures (Table S6) [13, 15-19, 57]. The well-developed hierarchical porosity can accelerate electrolyte permeation and shorten the distance of ions diffusion, and the improved electrical conductivity allows the rapid electron transport, which can effectively boost electrochemical kinetics.

Inspired by the improved rate behavior, the long-term cyclic test (Fig. 5i) over 1000 cycles at the large current density of 1.0 A g^{-1} has been performed after the initial several cycles at the low current of 0.1 A g^{-1}. The long-term cyclic property of BM-RH-SiO_2/C is the worst, in which the unstable capacity suffers from a successive decline from 315 mAh g^{-1} to 240 mAh g^{-1} at 400th cycle, finally only be 155 mAh g^{-1} at 1000th cycle. After N-doping modification, there are significant improvements in terms of the reversible capacity and cyclic stability regardless of RH-SiO_2/NC and BM-RH-SiO_2/NC. The former exhibits the highly reversible capacity of 404 mAh g^{-1} over 1000 cycles without obvious fluctuation, whereas the stable capacity of BM-RH-SiO_2/NC is up to 556 mAh g^{-1} with the Coulombic

efficiency of above 99%. The SEM images of corresponding worked electrodes of three samples after 1000 cycles are shown in Fig. S12. Compared with the distinct cracks of

BM- RH-SiO_2/C, BM-RH-SiO_2/NC still remains structural integrity, which is a convincing evidence of stably cyclic behavior.

Cyclic properties of the composites prepared under diverse urea usage and thermal temperatures at 0.1 and 1.0 A g^{-1} were also measured. As shown in Fig. S13, L-BM-RH-

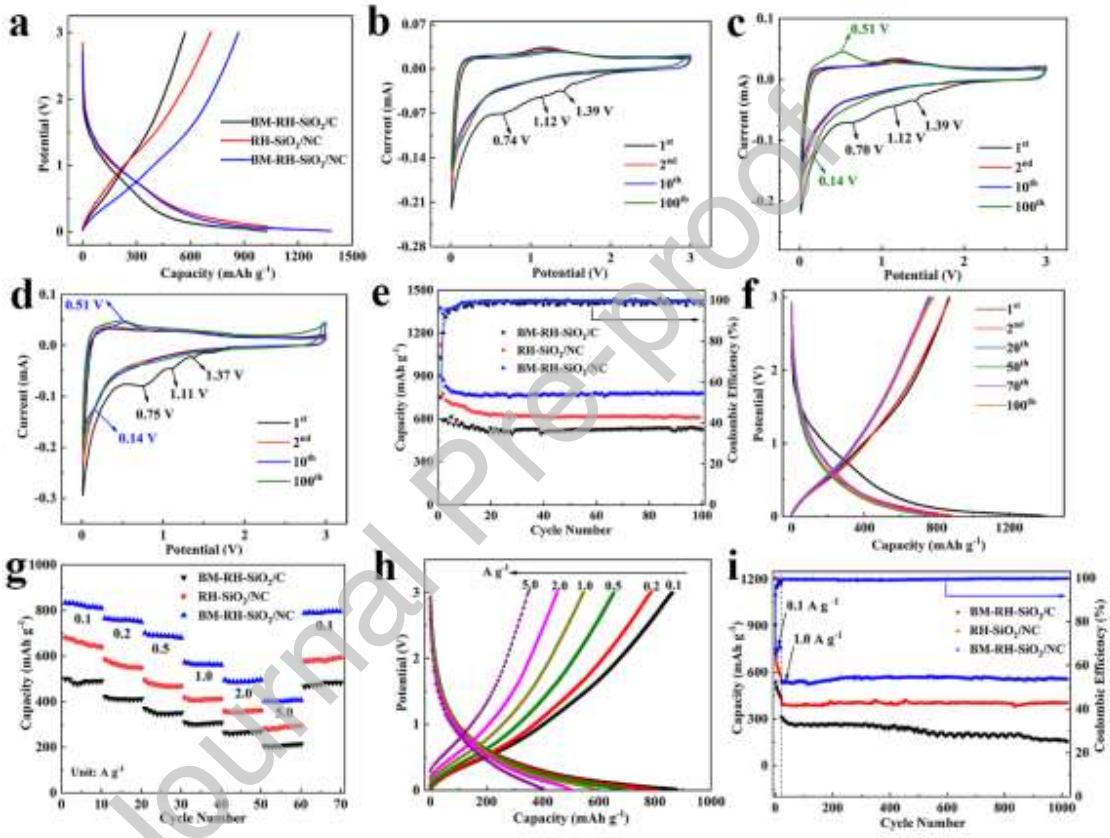

Fig. 5. (a) Change-discharge profiles of initial cycle of three samples; CV curves at different cycles of (b) BM-RH-SiO_2/C, (c) RH-SiO_2/NC and (d) BM-RH-SiO_2/NC; (e) cycling performances of three samples at 0.1 A g^{-1}; (f) voltage profiles of BM-RH-SiO_2/NC at various cycles; (g) rate capabilities of three samples from 0.1 A g^{-1}

to 5.0 A g^{-1}; (h) voltage profiles of BM-RH-SiO_2/NC at various current densities and (i) long-term cyclic properties of three samples at 1.0 A g^{-1} over 1000 cycles.

SiO_2/NC with the smallest content of N-nitrogen presents the worst cyclic behaviors in spite of 0.1 A $g^{-1}$and 1.0 A g^{-1}. The reversible capacity at 0.1 A g^{-1} of H-BM-RH-SiO_2/NC is as high as the one of BM-RH-SiO_2/NC, but the cyclic property at high rate of 1.0 A g^{-1} is slightly lower than that of BM-RH-SiO_2/NC, which may be attributed to the relatively poor mesoporous and microporous structure. As displayed in the Fig. S14, with the thermal temperature rising the cyclic performances of composites get worse regardless of 0.1 A $g^{-1}$and 1.0 A g^{-1}. It is worth noting that there appear to no significant distinction of the cyclic capability between BM-RH-SiO_2/NC-750 (3.91% for N) and BM-RH-SiO_2/NC-850(2.87% for N), especially at high rate of 1.0 A g^{-1}. Because the N-Q species with good electrical conductivity tends to be formed at high temperature, which guarantees Li-storage dynamics of whole electrode material at the high current. Summarily, the electrochemical performance of RH-SiO_2/N-doped carbon is dependent on the synergistic effect of the dispersion and particle sizes of SiO_2 and C, porous structure and the content and type of N-doping atoms.

The EIS measurement of BM-RH-SiO_2/C and BM-RH-SiO_2/NC after 1st and 100th cycle was shown in Fig. 6a. The Nyquist plot was used to study the Li-storage kinetics and mass transfer of electrode reaction, linked with the electrochemical performance, particularly the rate behavior and long-term cyclic capability. The semicircle of the curve

in the medium region represents the charge transfer resistor (R_{ct}). Obviously, the R_{ct} of the two samples are declining with the increasing cycles due to the activation process. As listed in Table S7, the R_{ct} of BM-RH-SiO_2/NC are simulated as 86.34 Ω and 21.10 Ω after the 1st

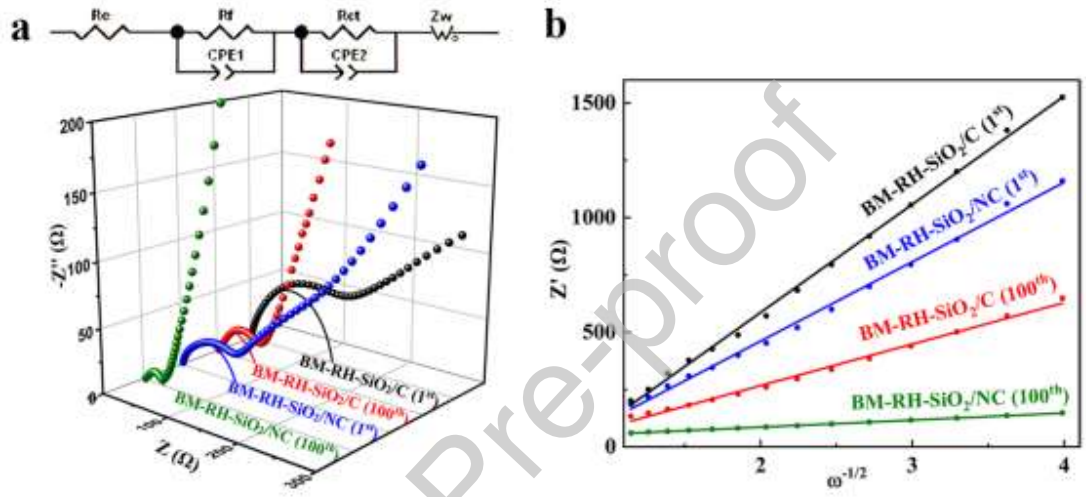

Fig. 6. (a) Nyquist plots, the fitted R_{ct} curves and equivalent circuit, and (b) the k values calculated by Z' versus $\omega^{-1/2}$ of BM-RH-SiO_2/C and BM-RH-SiO_2/NC after 1st and 100th cycle.

and 100th cycle based on the equivalent circuit, which are both smaller than that of BM-RH-SiO_2/C (132.45 Ω and 46.97 Ω). It means that BM-RH-SiO_2/NC is equipped with higher efficiency of electron transfer and ion diffusion, which is a manifestation of good kinetics. The straight line in low-frequency range refers to the Warburg impedance (Z_w) related to the Li^+ ions diffusion into the bulk material, which can be directly assessed by the lithium ions diffusion coefficient (D_{Li+}). From the Eq. (S1), the D_{Li+} is

inversely proportional to the Warburg factor (σ^2). According to the Eq. (S2) [58], the σ is the slope (κ) of line involving real resistance (Z') and square root of frequency ($\omega^{-1/2}$). As shown in Fig. 6b, the data from BM-RH-SiO_2/NC was fitted with the smaller κ values than BM-RH-SiO_2/C counterpart either 1st or 100th cycle. The D_{Li+}-values of BM-RH-SiO_2/C and BM-RH-SiO_2/NC after 100th cycle are calculated to be 8.52×10^{-13} and 3.07×10^{-11} cm^2 s^{-1}, respectively, meaning that the D_{Li+} of BM-RH-SiO_2/NC is 36 times as large as that of BM-RH-SiO_2/C. The lower charge transfer resistance and the faster lithium-ion diffusion of BM-RH-SiO_2/NC can contribute to the fast electrochemical dynamics during charge-discharge process, which benefits from the enhanced electronical conductivity, electrolyte wettability and hierarchical porosity.

The contrast of electrochemical performance with respect to the cyclic capability, high-rate property and long-term cyclic performance among all samples, a sensible fact is discovered that BM-RH-SiO_2/NC has the greater ability of Li^+ storage at the large rate, which might be clarified by the surface pseudocapacitive behavior [59]. CV curves of BM-RH-SiO_2/NC at varying scan rates from 0.2 to 1.5 mV s^{-1} were presented in Fig. 7a to further explore the dynamic process, where the current (*i*) obeys the law as shown in the following Eq. (4) or Eq. (5). The *a* and *b* are an adjustable parameter, and *v* is sweep rate:

$$i = av^b \quad (4)$$

or

$$\log(i) = \log(a) + b\log(v) \quad (5)$$

Here, the *b*-value is equal to 0.5 manifesting a completely ionic diffusion-controlled process and the *b*-value of 1.0 belongs to a total capacitive-controlled process or surface pseudocapacitive behavior [58]. Base on the Eq. (4), the *b*-value for anodic peaks of BM-RH-SiO_2/NC is the slope of fitted line and can be determined as 0.76 (Fig. 7b), implying the current contribution is dominated by surface capacitive effect which is a faster kinetics.

$$i(v) = \kappa_1 v + \kappa_2 v^{1/2} \quad (6)$$

As described by the Eq. (6), the values of current contribution stemming from the capacitive-controlled part and diffusion-controlled part can be further quantified by $\kappa_1 v$ and the $\kappa_2 v^{1/2}$, respectively [58]. As given in Fig. 7c, when the sweep rate is 1.5 mV s^{-1}, the capacitive fraction accounts for 75.83% of total capacity that is a feature of fast kinetics. Moreover, the contribution ratios of capacitive part at varying scan rates from 0.2 mV s^{-1} to 1.5 mV s^{-1} were estimated and listed in Fig. 7d. Noticeably, the capacitive contribution

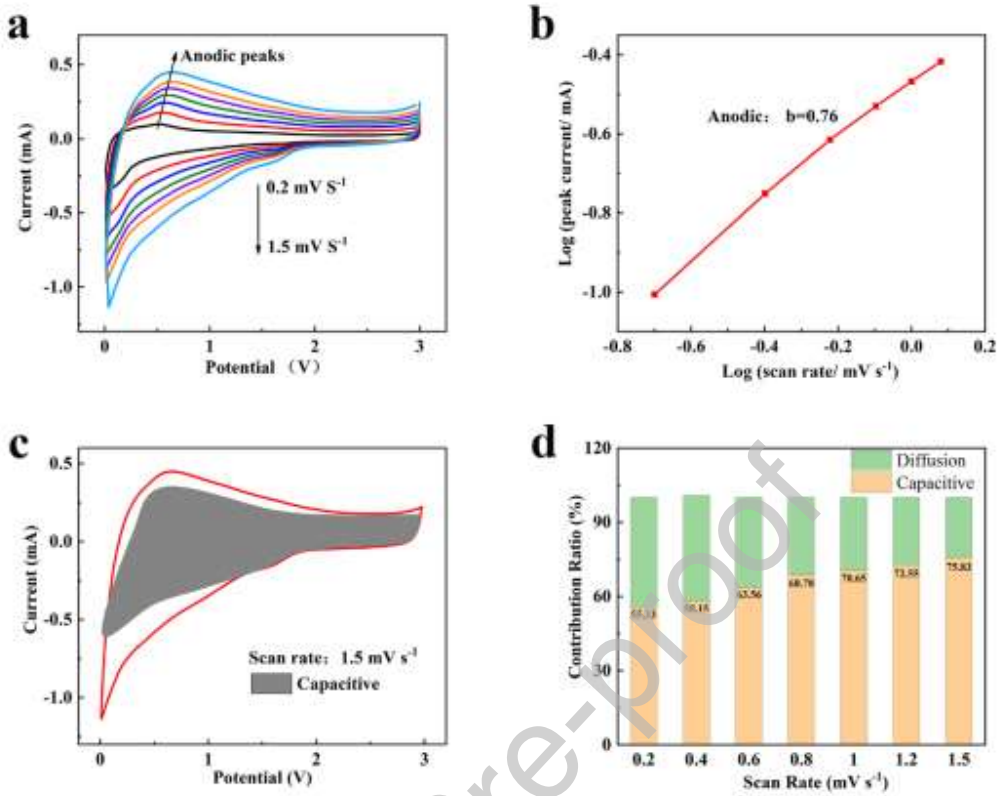

Fig. 7. BM-RH-SiO_2/NC: (a) CV curves at various scan rates from 0.2 to 1.5 mV s^{-1}; (b) log (peak current) versus log (scan rate) profile to estimate the b-value; (c) CV curve containing the capacitive contribution section drawn in gray at 1.5 mV s^{-1} and (d) the bar graph involving the percentage of capacitive contribution ratio at various scan rates.

ratio is gradually ascending as the increasing scan rate, reasonably validating that the faster

kinetics of BM-RH-SiO_2/NC can meet the demand of the high-rate performance and of long-term cyclic property at high current density.

4. Conclusion

In summary, BM-RH-SiO_2/NC composites with hierarchically porous structure have been prepared by ball mill and thermal treatment, where the natural SiO_2 nanoparticles are homogeneously coated by the N-doped carbon layer. The volume expansion can be effectively relieved by the uniform NC layer during Li-insertion/desertion process and then the stably cyclic performance has been achieved. The hierarchical porosity of BM-RH-SiO_2/NC plays a crucial role in increasing active sites for Li storage and providing the rapid Li^+-diffusion channel. Furthermore, the N-doping improves the electrical conductivity and electrolyte wettability of electrode materials. As the anodes, the BM-RH-SiO_2/NC delivers a reversible capacity of 780 mAh g^{-1} after 100 cycles at the current density of 0.1 A g^{-1}. When the large rate is 1.0 A g^{-1} it exhibits a stable capacity of 556 mAh g^{-1} over 1000 cycles, and a high capacity of 402 mAh g^{-1} is still achievable at the rate of 5.0 A g^{-1}. These demonstrate an outstanding long-term cyclic performance and high-rate capability. Importantly, the unique and preferable Li-storage mechanism of active SiO_2 in BM-RH-SiO_2/NC has been found and it is the fast kinetics that can accommodate the excellent Li-storage capability at high rate. The achievements in scalable preparation strategy, facile N-doping modification and significantly enhanced electrochemical performance are expected to promote the further development on RHs-based SiO_2/C composite anode materials for LIBs.

Declaration of Competing Interest

The authors declare no competing financial interest.

Acknowledgements

We are grateful to the financial support from Graduate Innovation Fund of Jilin University (No. 101832018C176).

Supporting Information

The Supporting Information is available.

References

[1] K. Amine, I. Belharouak, Z. Chen, T. Tran, H. Yumoto, N. Ota, S.-T. Myung, Y.-K. Sun, Nanostructured anode material for high-power battery system in electric vehicles, Adv. Mater., 22 (2010) 3052-3057.

[2] M. Armand, J.M. Tarascon, Building better batteries, Nature, 451 (2008) 652-657.

[3] Y. Feng, X. Liu, L. Liu, Z. Zhang, Y. Teng, D. Yu, J. Sui, X. Wang, SiO_2/c composite derived from rice husks with enhanced capacity as anodes for lithium-ion batteries, ChemistrySelect, 3 (2018) 10338-10344.

[4] J.B. Goodenough, Electrochemical energy storage in a sustainable modern society, Energ. Environ. Sci., 7 (2014) 14-18.

[5] J. Ou, Y. Zhang, L. Chen, H. Yuan, D. Xiao, Heteroatom doped porous carbon derived from hair as an anode with high performance for lithium ion batteries, RSC Adv., 4 (2014) 63784-63791.

[6] M. Sasidharan, D. Liu, N. Gunawardhana, M. Yoshio, K. Nakashima, Synthesis, characterization and application for lithium-ion rechargeable batteries of hollow silica nanospheres, J. Mater. Chem., 21 (2011) 13881-13888.

[7] H. Wang, P. Wu, H. Shi, W. Tang, Y. Tang, Y. Zhou, P. She, T. Lu, Hollow porous silicon oxide nanobelts for high-performance lithium storage, J. Power Sources, 274 (2015) 951-956.

[8] J. Cui, J. Yang, J. Man, S. Li, J. Yin, L. Ma, W. He, J. Sun, J. Hu, Porous Al/Al_2O_3 two-phase nanonetwork to improve electrochemical properties of porous C/SiO_2 as anode for Li-ion batteries, Electrochim. Acta, 300 (2019) 470-481.

[9] R. Wang, X. Dai, Z. Qian, S. Zhong, S. Chen, S. Fan, H. Zhang, F. Wu, Boosting lithium storage in free-standing black phosphorus anode via multifunction of nanocellulose, ACS Appl. Surf. Sci., 12 (2020) 31628-31636.

[10] Z. Liu, Q. Yu, Y. Zhao, R. He, M. Xu, S. Feng, S. Li, L. Zhou, L. Mai, Silicon oxides: a promising family of anode materials for lithium-ion batteries, Chem. Soc. Rev., 48 (2019) 285-309.

[11] C. Zhu, D. Wei, Y. Wu, Z. Zhang, G. Zhang, J. Duan, L. Li, H. Zhu, Z. Zhu, Z. Chen, Controllable construction of interconnected SnO_x/N-doped carbon/carbon composite for enhanced-performance lithium-ion batteries anodes, J. Alloy. Compd., 778 (2019) 731-740.

[12] W.-S. Chang, C.-M. Park, J.-H. Kim, Y.-U. Kim, G. Jeong, H.-J. Sohn, Quartz (SiO_2): a new energy storage anode material for Li-ion batteries, Energ. Environ. Sci., 5 (2012) 6895-6899.

[13] P. Lv, H. Zhao, J. Wang, X. Liu, T. Zhang, Q. Xia, Facile preparation and electrochemical properties of amorphous SiO_2/C composite as anode material for lithium ion batteries, J. Power Sources, 237 (2013) 291-294.

[14] H. Wang, P. Wu, M. Qu, L. Si, Y. Tang, Y. Zhou, T. Lu, Highly reversible and fast lithium storage in graphene-wrapped SiO_2 nanotube network, ChemElectroChem, 2 (2015) 508-511.

[15] M. Li, Y. Yu, J. Li, B. Chen, X. Wu, Y. Tian, P. Chen, Nanosilica/carbon composite spheres as anodes in Li-ion batteries with excellent cycle stability, J. Mater. Chem. A, 3 (2015) 1476-1482.

[16] S. Wang, N. Zhao, C. Shi, E. Liu, C. He, F. He, L. Ma, In-situ grown CNTs modified SiO_2/C composites as anode with improved cycling stability and rate capability for lithium storage, Appl. Surf. Sci., 433 (2018) 428-436.

[17] C. Nita, J. Fullenwarth, L. Monconduit, J.-M. Le Meins, P. Fioux, J. Parmentier, C.M. Ghimbeu, Eco-friendly synthesis of SiO_2 nanoparticles confined in hard carbon: A promising material with unexpected mechanism for Li-ion batteries, Carbon, 143 (2019) 598-609.

[18] C. Liang, Y. Chen, H. Xu, Y. Xia, X. Hou, Y. Gan, X. Ma, X. Tao, H. Huang, J. Zhang, W. Han, W. Zhang, Embedding submicron SiO_2 into porous carbon as advanced lithium-ion batteries anode with ultralong cycle life and excellent rate capability, J. Taiwan Inst. Chem. E., 95 (2019) 227-233.

[19] Y. Mao, H. Duan, B. Xu, L. Zhang, Y. Hu, C. Zhao, Z. Wang, L. Chen, Y. Yang, Lithium storage in nitrogen-rich mesoporous carbon materials, Energ. Environ. Sci., 5 (2012) 7950-7955.

[20] X. Liu, J. Zhang, S. Guo, N. Pinna, Graphene/N-doped carbon sandwiched nanosheets with ultrahigh nitrogen doping for boosting lithium-ion batteries, J. Mater. Chem. A, 4 (2016) 1423-1431.

[21] C. Zhan, X. Yu, Q. Liang, W. Liu, Y. Wang, R. Lv, Z.-H. Huang, F. Kang, Flour food waste derived activated carbon for high-performance supercapacitors, RSC Adv., 6 (2016) 89391-89396.

[22] J. Entwistle, A. Rennie, S. Patwardhan, A review of magnesiothermic reduction of silica to porous silicon for lithium-ion battery applications and beyond, J. Mater. Chem. A, 6 (2018) 18344-18356.

[23] W.C. Cho, H.J. Kim, H.I. Lee, M.W. Seo, H.W. Ra, S.J. Yoon, T.Y. Mun, Y.K. Kim, J.H. Kim, B.H. Kim, J.W. Kook, C.-Y. Yoo, J.G. Lee, J.W. Choi, 5L-scale magnesio-milling reduction of nanostructured SiO_2 for high capacity silicon anodes in lithium-ion batteries, Nano Lett., 16 (2016) 7261-7269.

[24] D.S. Jung, M.-H. Ryou, Y.J. Sung, S.B. Park, J.W. Choi, Recycling rice husks for high-capacity lithium battery anodes, Proc. Natl. Acad. Sci. U. S. A., 110 (2013) 12229-12234.

[25] X. Zhang, Y. Li, D. Li, J. Xiao, W. Zhang, Y. Xu, Rice husk derived porous carbon decorated with hierarchical molybdenum disulfide microflowers: Synergistic lithium storage performance and lithiation kinetics, Int. J. Hydrogen Energ., 44 (2019) 7438-7447.

[26] J. Cui, H. Zhang, Y. Liu, S. Li, W. He, J. Hu, J. Sun, Facile, economical and environment-friendly synthesis process of porous N-doped carbon/SiO_x composite from rice husks as high-property anode for Li-ion batteries, Electrochim. Acta, 334 (2020) 135619.

[27] X. Fan, B. Yin, T. Wu, M. Feng, G.C. Zhang, S. Li, S. Tang, J. Gu, B. Wen, L. Lu, Rice husk-based 3D porous silicon/carbon nanocomposites as anode for lithium-ion batteries, Energy Technol., 7 (2019) 1800787.

[28] J. Liang, J. Zhao, Y. Li, K.-T. Lee, C. Liu, H. Lin, Q. Cheng, Q. Lan, L. Wu, S. Tang, L. An, Y.-C. Cao, In situ SiO_2 etching strategy to prepare rice husk-derived porous carbons for supercapacitor application, J. Taiwan Inst. Chem. E., 81 (2017) 383-390.

[29] Y.-C. Zhang, Y. You, S. Xin, Y.-X. Yin, J. Zhang, P. Wang, X.-s. Zheng, F.-F. Cao, Y.-G. Guo, Rice husk-derived hierarchical silicon/nitrogen-doped carbon/carbon nanotube spheres as low-cost and high-capacity anodes for lithium-ion batteries, Nano Energy, 25 (2016) 120-127.

[30] P. Balaz, M. Achimovicova, M. Balaz, P. Billik, Z. Cherkezova-Zheleva, J. Manuel Criado, F. Delogu, E. Dutkova, E. Gaffet, F. Jose Gotor, R. Kumar, I. Mitov, T. Rojac, M. Senna, A. Streletskii, K. Wieczorek-Ciurowa, Hallmarks of mechanochemistry: from nanoparticles to technology, Chem. Soc. Rev., 42 (2013) 7571-7637.

[31] C. Bolm, J.G. Hernandez, Mechanochemistry of Gaseous Reactants, Angew. Chem. Int. Edit., 58 (2019) 3285-3299.

[32] Z.Q. Li, C.J. Lu, Z.P. Xia, Y. Zhou, Z. Luo, X-ray diffraction patterns of graphite and turbostratic carbon, Carbon, 45 (2007) 1686-1695.

[33] H.B. Yang, J. Miao, S.-F. Hung, J. Chen, H.B. Tao, X. Wang, L. Zhang, R. Chen, J. Gao, H.M. Chen, L. Dai, B. Liu, Identification of catalytic sites for oxygen reduction and oxygen evolution in N-doped graphene materials: Development of highly efficient metal-free bifunctional electrocatalyst, Sci. Adv., 2 (2016) e1501122.

[34] B. Guo, Q. Liu, E. Chen, H. Zhu, L. Fang, J.R. Gong, Controllable N-doping of graphene, Nano Lett., 10 (2010) 4975-4980.

[35] Q. Pan, F. Zheng, X. Ou, C. Yang, X. Xiong, M. Liu, MoS_2 encapsulated SnO_2-SnS/C nanosheets as a high performance anode material for lithium ion batteries, Chem. Eng. J., 316 (2017) 393-400.

[36] A. Belgibayeva, I. Taniguchi, Synthesis and characterization of SiO_2/C composite nanofibers as free-standing anode materials for Li-ion batteries, Electrochim. Acta, 328 (2019) 135101.

[37] S.-S. Lee, C.-M. Park, Amorphous silicon dioxide-based composites for high-performance Li-ion battery anodes, Electrochim. Acta, 284 (2018) 220-225.

[38] L. Li, P. Liu, K. Zhu, J. Wang, G. Tai, J. Liu, Flexible and robust N-doped carbon nanofiber film encapsulating uniformly silica nanoparticles: Free-standing long-life and low-cost electrodes for Li-and Na-ion batteries, Electrochim. Acta, 235 (2017) 79-87.

[39] H. Lu, R. Chen, Y. Hu, X. Wang, Y. Wang, L. Ma, G. Zhu, T. Chen, Z. Tie, Z. Jin, J. Liu, Bottom-up synthesis of nitrogen-doped porous carbon scaffolds for lithium and sodium storage, Nanoscale, 9 (2017) 1972-1977.

[40] L. Qie, W. Chen, X. Xiong, C. Hu, F. Zou, P. Hu, Y. Huang, Sulfur-doped carbon with enlarged interlayer distance as a high-performance anode material for sodium-ion batteries, Adv. Sci., 2 (2015) 1500195.

[41] Y. Jiang, D. Mu, S. Chen, B. Wu, Z. Zhao, Y. Wu, Z. Ding, F. Wu, Hollow silica spheres with facile carbon modification as an anode material for lithium-ion batteries, J. Alloy. Compd., 744 (2018) 7-14.

[42] D. Wei, Y. Liu, Y. Wang, H. Zhang, L. Huang, G. Yu, Synthesis of N-doped graphene by chemical vapor deposition and its electrical properties, Nano Lett., 9 (2009) 1752-1758.

[43] Y. Jiao, Y. Zheng, M. Jaroniec, S.Z. Qiao, Origin of the electrocatalytic oxygen reduction activity of graphene-based catalysts: a roadnnap to achieve the best performance, J. Am. Chem. Soc., 136 (2014) 4394-4403.

[44] Y. Zheng, Y. Jiao, Y. Zhu, L.H. Li, Y. Han, Y. Chen, A. Du, M. Jaroniec, S.Z. Qiao, Hydrogen evolution by a metal-free electrocatalyst, Nature Commun., 5 (2014) 4783.

[45] W. Ren, D. Li, H. Liu, R. Mi, Y. Zhang, L. Dong, L. Dong, Lithium storage performance of carbon nanotubes with different nitrogen contents as anodes in lithium ions batteries, Electrochim. Acta, 105 (2013) 75-82.

[46] K.-l. Hong, L. Qie, R. Zeng, Z.-q. Yi, W. Zhang, D. Wang, W. Yin, C. Wu, Q.-j. Fan, W.-x. Zhang, Y.-h. Huang, Biomass derived hard carbon used as a high performance anode material for sodium ion batteries, J. Mater. Chem. A, 2 (2014) 12733-12738.

[47] Q.L. Hu, H. Suzuki, H. Gao, H. Araki, W. Yang, T. Noda, High-frequency FTIR absorption of SiO_2/Si nanowires, Chem. Phys. Lett., 378 (2003) 299-304.

[48] M. Sarangi, P. Nayak, T.N. Tiwari, Effect of temperature on nano-crystalline silica and carbon composites obtained from rice-husk ash, Compos. Part B-Eng., 42 (2011) 1994-1998.

[49] S.N. Talapaneni, G.P. Mane, A. Mano, C. Anand, D.S. Dhawale, T. Mori, A. Vinu, Synthesis of nitrogen-rich mesoporous carbon nitride with tunable pores, band gaps and nitrogen content from a single aminoguanidine precursor, ChemSusChem, 5 (2012) 700-708.

[50] A.M. Andersson, D.P. Abraham, R. Haasch, S. MacLaren, J. Liu, K. Amine, Surface characterization of electrodes from high power lithium-ion batteries, J. Electrochem. Soc., 149 (2002) A1358-A1369.

[51] J. Ou, Y. Zhang, L. Chen, Q. Zhao, Y. Meng, Y. Guo, D. Xiao, Nitrogen-rich porous carbon derived from biomass as a high performance anode material for lithium ion batteries, J. Mater. Chem. A, 3 (2015) 6534-6541.

[52] X. Ao, H. Sun, C. Wang, J. Li, Y. Ruan, B. Li, Q.-H. Wu, Y. Li, J. Jiang, Y. Yang, L. Mai, In situ nitrogen-doped helical mesoporous carbonaceous nanotubes for superior-high lithium anodic performance, Carbon, 130 (2018) 599-606.

[53] P. Hao, Z. Zhao, Y. Leng, J. Tian, Y. Sang, R.I. Boughton, C.P. Wong, H. Liu, B. Yang, Graphene-based nitrogen self-doped hierarchical porous carbon aerogels derived from chitosan for high performance supercapacitors, Nano Energy, 15 (2015) 9-23.

[54] J. Tu, Y. Yuan, P. Zhan, H. Jiao, X. Wang, H. Zhu, S. Jiao, Straightforward approach toward SiO_2 nanospheres and their superior lithium storage performance, J. Phys. Chem. C, 118 (2014) 7357-7362.

[55] W. Wu, M. Wang, J. Wang, C. Wang, Y. Deng, Green design of $Si/SiO_2/C$ composites as high-performance anodes for lithium-ion batteries, Acs Appl. Energy Mater., 3 (2020) 3884-3892.

[56] Z. Yang, Y. Du, G. Hou, Y. Ouyang, F. Ding, F. Yuan, Nanoporous silicon spheres preparation via a controllable magnesiothermic reduction as anode for Li-ion batteries, Electrochim. Acta, 329 (2020) 135141.

[57] X. Yang, H. Huang, Z. Li, M. Zhong, G. Zhang, D. Wu, Preparation and lithium-storage performance of carbon/silica composite with a unique porous bicontinuous nanostructure, Carbon, 77 (2014) 275-280.

[58] F. Zheng, W. Zhong, Q. Deng, Q. Pan, X. Ou, Y. Liu, X. Xiong, C. Yang, Y. Chen, M. Lite, Three-dimensional (3D) flower-like $MoSe_2$/N-doped carbon composite as a long-life and high-rate anode material for sodium-ion batteries, Chem. Eng. J., 357 (2019) 226-236.

[59] X. Yang, R.-Y. Zhang, J. Zhao, Z.-X. Wei, D.-X. Wang, X.-F. Bie, Y. Gao, J. Wang, F. Du, G. Chen, Amorphous tin-based composite oxide: A high-rate and ultralong-life sodium-ion-storage material, Adv. Energy Mater., 8 (2018) 1701827.